Journal of Materials Chemistry A

ROYAL SOCIETY OF CHEMISTRY

PAPER

View Article Online
View Journal | View Issue

Check for updates

Cite this: J. Mater. Chem. A, 2026, 14, 637

Liquid metal eutectic gallium–indium (EGaIn) blended with paraffinic wax for enhanced solar-to-heat conversion

Hyeonmin Jo,†[a] Somnath Chowdhury,†[b] Chimin Song,†[a] Eunju Na,[a] Minjeong Cho,[a] Sung Gu Kang*[b] and Joohyung Lee *[a]

Eutectic gallium–indium (EGaIn) has emerged as a promising liquid metal (LM) photothermal material but suffers from poor broadband absorption, limiting its potential in solar energy harvesting. Here, we demonstrate that blending EGaIn with *n*-eicosane ($C_{20}H_{42}$), a chemically inert paraffin-based phase change material (PCM), substantially enhances broadband solar-to-heat conversion. Although $C_{20}H_{42}$ alone exhibits negligible solar absorption and no intrinsic photothermal activity, its physical hybridization with EGaIn enables more effective utilization of incident light by forming a thick dielectric layer on the plasmonic LM surface. The resulting EGaIn–$C_{20}H_{42}$ hybrid particles display progressively reduced reflectance across the UV-visible-NIR spectrum as the $C_{20}H_{42}$ content increases, leading to markedly improved photothermal heating under simulated solar irradiation. Compared with pure EGaIn droplets ($\Delta T \approx 7$ °C after 20 min), $C_{20}H_{42}$-rich hybrids achieved ΔT values up to 19.9 °C despite containing less metallic EGaIn. Differential scanning calorimetry confirmed that $C_{20}H_{42}$ preserved its PCM functionality within the hybrids, exhibiting latent heat storage and release near 30–40 °C, which produced characteristic temperature plateaus during heating and cooling cycles. These synergistic effects enable hybrids that simultaneously enhance sensible heat generation and latent heat utilization without chemical modification of the constituents. This blending strategy thus provides a simple, non-reactive route to boost LM-mediated solar energy harvesting, demonstrating the potential of multifunctional LM–PCM composites in thermal management, energy storage, and solar-driven technologies.

Received 12th September 2025
Accepted 17th November 2025

DOI: 10.1039/d5ta07484c

rsc.li/materials-a

Open Access Article. Published on 17 November 2025. Downloaded on 3/3/2026 11:12:49 AM. This article is licensed under a Creative Commons Attribution 3.0 Unported Licence.

Introduction

The Sun serves as the fundamental source of energy for virtually all biological and environmental processes on Earth. It emits electromagnetic radiation across the ultraviolet (UV), visible, and infrared (IR) regions of the spectrum, each characterized by distinct wavelength ranges. Upon absorption by matter, these radiations can be converted into thermal energy, a process referred to as photothermal conversion.[1] Solar-driven photothermal conversion has garnered increasing attention due to its significance in a wide range of applications, such as thermal energy harvesting,[2,3] solar steam generation,[4,5] water purification,[5–7] electricity generation,[5,8,9] and de/anti-icing.[10,11] Various materials have been studied that enable high absorption of broad-spectrum light and efficient conversion of this light into heat, including metals,[2,5] semiconductors,[5,6] carbon,[3,7–9,11] organic polymers,[4,10] and their composites.[12,13] Each of these materials can induce photothermal conversion through different mechanisms. Metallic nanomaterials convert light into heat through localized surface plasmon resonance (LSPR) phenomena,[14] which operate over relatively narrow wavelength ranges.[1] Semiconductor materials absorb light with photon energies comparable to their bandgaps, generating electron–hole pairs; the energy of the excited electrons is then converted into heat *via* non-radiative relaxation processes.[15] Carbon-based materials and certain organic polymers efficiently convert absorbed light into heat *via* lattice vibrations.[1]

Gallium–indium eutectic alloy (EGaIn), a type of liquid metal (LM)[16] with a low melting point (~16 °C), has recently emerged as a promising photothermal conversion material.[17–23] Over the past decade, a significant number of studies have reported that the unique combination of its plasmonic properties and its soft, deformable nature near room temperature enables it to function as a shape-transformable photothermal transducer. Notably, unlike the well-known LM mercury, EGaIn is significantly less toxic, which has spurred extensive research into its biomedical applications, such as photothermal therapy[17–19] and drug delivery systems.[20,21] Early studies discussed the plasmonic resonance of EGaIn under UV light; however, more recent research, particularly in the biomedical field, has focused on

[a]Department of Chemical Engineering, Myongji University, 116 Myongji-ro, Cheoin-gu, Yongin-si, Gyeonggi-do, 17058, Korea. E-mail: sgkang@ulsan.ac.kr; ljbro@mju.ac.kr
[b]School of Chemical Engineering, University of Ulsan, 93 Daehak-ro, Nam-gu, Ulsan-si, 44610, Korea
† These authors contributed equally to this work.

Open Access Article. Published on 17 November 2025. Downloaded on 3/3/2026 11:12:49 AM. This article is licensed under a Creative Commons Attribution 3.0 Unported Licence.

the photothermal conversion properties of EGaIn—especially when dispersed as micro[21,22] or nanoscale[17–20,23] colloidal droplets—under near-infrared (NIR) light. Although simulation-based efforts to elucidate the plasmonic properties of EGaIn across a broad wavelength range from UV to NIR have been reported recently,[24] a much greater number of experimental observations are still urgently needed.

Research on solar-driven applications using EGaIn is relatively scarce, primarily due to the limited solar absorption capability of pure EGaIn. To harness EGaIn for solar applications, its hybridization with other materials has been considered essential.[5,12,13,24–28] For instance, Wei and colleagues mixed stearic acid (STA) with EGaIn *via* high-energy ball milling, inducing a mechanochemical reaction.[5] They proposed that this process forms a new chemical bond between STA and EGaIn, which significantly narrows the bandgap of EGaIn. The resulting STA–EGaIn hybrid demonstrated improved solar-to-thermal conversion efficiency and was employed in applications such as solar steam generation, desalination, and electricity production. Meanwhile, Flores and colleagues developed a high-performance thermoelectric device by fabricating a broadband light absorber ink based on metal-polyphenol coordination complexes (MPI) and depositing it onto a surface coated with gallium (Ga) droplets, which, similar to EGaIn, exhibit excellent NIR absorption along with high thermal and electrical conductivity.[13] Notably, no evidence for the formation of new compounds at the MPI–Ga interface was observed using this method. The two distinct layers in the resulting MPI–Ga bilayer composite appeared to serve different roles. Broadband light absorption predominantly occurred in the outer MPI layer directly exposed to solar irradiation, which constituted the primary mechanism driving the enhanced solar-to-thermal conversion of the composite.

Most previous studies that employed LMs for solar energy harvesting have thus relied on inducing irreversible chemical reactions of the LM or coupling it with strongly light-absorbing materials.[5,12,13,25–29] In contrast, mechanisms for enhancing photothermal conversion efficiency through simple hybridization with chemically inert and optically non-absorbing materials possessing structurally simple compositions remain largely unexplored. Typical solar-driven applications such as water harvesting[30,31] and passive thermal management[32] ultimately require large-area implementation. However, the relatively high cost of LM can be a major hurdle for practical deployment. Furthermore, strategies that rely on specialty chemicals or complex multistep reactions to improve photothermal conversion efficiency tend to increase production costs and move LM-based technologies further away from real-world feasibility. Therefore, exploring scalable materials that are commercially accessible and easily hybridized with LMs is not only of fundamental scientific importance but can also provide a valuable conceptual guideline for the rational design of plasmonic LM-based photothermal systems for diverse future applications.

In this study, we report the enhanced solar-to-heat conversion observed in EGaIn blended with *n*-eicosane ($C_{20}H_{42}$), a type of paraffin wax. This material possesses a chemically simple structure, is relatively inexpensive, and is thus favorable for scalable applications. Very recently, a similar composite system combining mixed paraffin waxes with LM was reported;[29] however, that study incorporated strongly light-absorbing graphene nanoplatelets for specific thermoelectric generation applications, making it difficult to isolate the intrinsic synergistic effect between the LM and paraffin components on photothermal conversion. Furthermore, it remains essential to investigate the photothermal behavior of LM–paraffin composites under more realistic solar irradiation conditions (1 SUN, 1 kW m^{-2}) rather than the impractically high intensities previously employed, in order to elucidate their intrinsic light-to-heat conversion characteristics and practical applicability. While $C_{20}H_{42}$ does not form new bulk compounds with EGaIn, it can create a thick dielectric layer on the metallic surface, modifying its optical properties. Although $C_{20}H_{42}$ itself exhibits limited broadband solar absorption and lacks intrinsic photothermal activity, the physically hybridized paraffin layer markedly reduces the direct reflection of incident broadband light from the plasmonic EGaIn surface, thereby enabling substantially enhanced solar-to-heat conversion. Another key characteristic of $C_{20}H_{42}$ is its phase change material (PCM) properties,[22,33] which undergo solid–liquid transitions in the temperature range of 30–40 °C. In these temperatures, it can absorb (when heated) or release (when cooled) significant amounts of heat in the form of latent heat. This characteristic makes it a promising passive thermal management material, with potential applications ranging from traditional areas such as building materials[34] and textiles[35] to newer fields like batteries,[36] solar cells,[37] and cosmetics.[38] Although extensive studies have explored the integration of plasmonic absorbers with PCMs to harvest solar or photothermal energy through latent heat storage,[39] there has been little investigation into the synergistic combination of PCMs with deformable, liquid-state photothermal agents such as LMs—which could open new opportunities for multifunctional and adaptive energy-harvesting systems.[24] When the surface temperature rises *via* LM-mediated photothermal conversion to near or above the melting temperature of $C_{20}H_{42}$ due to photothermal heating, the generated heat is stored as latent heat in $C_{20}H_{42}$. When the heated surface cools to near or below the crystallization temperature of $C_{20}H_{42}$, the stored latent heat is released. These latent heat storage and release capabilities increase with the proportion of $C_{20}H_{42}$ in the hybrid material. Consequently, when the content of EGaIn, the photothermal agent actually converting sunlight to heat, is low in the hybrid composition, a paradoxically much higher temperature rise (*i.e.*, sensible heat effect) can be expected, along with enhanced latent heat utilization. We discuss this unique potential of hybridizing the LM EGaIn with paraffin-based PCMs, which are generally considered to be chemically inert and exhibit low solar absorption, for solar energy harvesting.

Results and discussion

Fig. 1a illustrates the appearance of mixtures of EGaIn and $C_{20}H_{42}$ at various volume ratios. Pure EGaIn, with a melting

 This journal is © The Royal Society of Chemistry 2026

Open Access Article. Published on 17 November 2025. Downloaded on 3/3/2026 11:12:49 AM.
This article is licensed under a Creative Commons Attribution 3.0 Unported Licence.

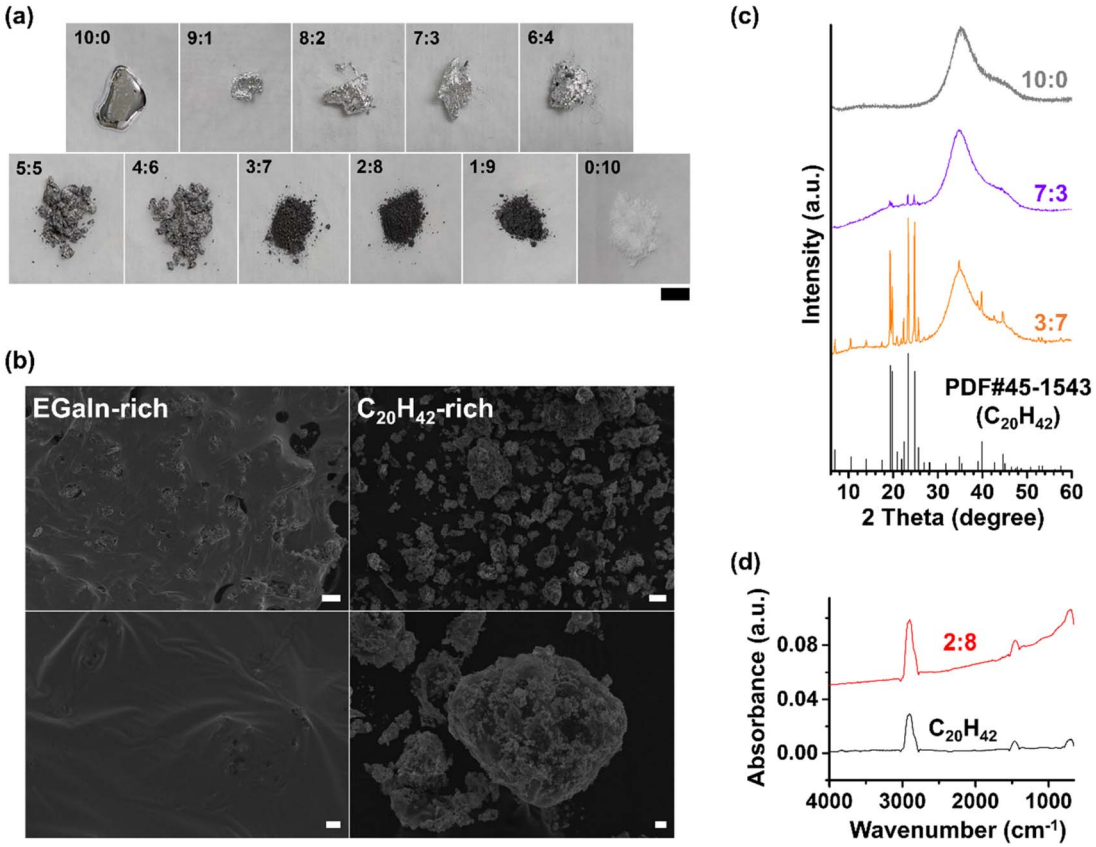

Fig. 1 (a) Appearances of precursor mixtures of EGaIn and $C_{20}H_{42}$ with various EGaIn : $C_{20}H_{42}$ volume ratios (scale bar: 1 cm). (b) SEM images of EGaIn-rich (8 : 2; left column) and $C_{20}H_{42}$-rich (2 : 8; right column) precursor mixtures (scale bars in the upper and lower rows correspond to 100 μm and 10 μm, respectively). (c) XRD patterns of pure EGaIn (10 : 0), EGaIn-rich (7 : 3) precursor mixture, and $C_{20}H_{42}$-rich' (3 : 7) precursor mixture, along with the standard PDF card of $C_{20}H_{42}$. (d) ATR-FTIR spectra of pure $C_{20}H_{42}$ (0 : 10) and $C_{20}H_{42}$-rich (2 : 8) precursor mixture. Both spectra were smoothed to improve signal-to-noise ratios.

point of approximately 16 °C,[16] exists as a low-viscosity liquid at room temperature, and being metallic, exhibits a bright, reflective appearance. In contrast, $C_{20}H_{42}$, a paraffinic wax with a melting point of approximately 37–39 °C,[38] appears as a white solid powder at room temperature. When these two materials were mixed in various proportions using a porcelain mortar and pestle, the resulting mixtures exhibited different characteristics depending on the EGaIn-to-$C_{20}H_{42}$ ratio. In the range of 9 : 1 to 6 : 4 EGaIn : $C_{20}H_{42}$ by volume, the mixtures retained a metallic luster but formed a highly viscous paste compared to pure EGaIn. This behavior aligns with our previous observations on mixtures where a similar paraffinic substance, *n*-docosane ($C_{22}H_{46}$), was micronized and dispersed into an EGaIn matrix at volume fractions up to 40 vol%.[33] At higher $C_{20}H_{42}$ volume fractions, specifically in the range of 5 : 5 to 4 : 6 EGaIn : $C_{20}H_{42}$, the mixtures exhibited a texture resembling wet sand, with significantly diminished brightness and reflectivity. Finally, for $C_{20}H_{42}$-rich mixtures with EGaIn : $C_{20}H_{42}$ volume ratios from 3 : 7 to 1 : 9, the mixtures resulted in dark solid powders.

The transition in the morphology of LM and solid powder mixtures from a liquid-like to a solid-like state with increasing solid powder content is a phenomenon commonly observed in mixtures of LMs with solid powders,[40,41] including substances other than paraffinic compounds like $C_{20}H_{42}$ used in this study. In the typical scanning electron microscope (SEM) images of EGaIn-rich mixtures (*e.g.*, those with EGaIn : $C_{20}H_{42}$ volume ratios of 9 : 1–6 : 4; Fig. 1b, left), the bulk LM appeared to form a "continuous phase," in the colloidal sense, seemingly enveloping small particulates, presumably $C_{20}H_{42}$. The corresponding X-ray diffraction (XRD) patterns of these mixtures (Fig. 1c) showed only very weak peaks attributable to $C_{20}H_{42}$, while exhibiting broad peaks resembling those of bulk LM. This observation suggested that the majority of $C_{20}H_{42}$ was incorporated into the bulk LM. This continuous phase of LM accounts for the shiny and reflective appearance observed in the mixture. In contrast, the SEM images of the $C_{20}H_{42}$-rich mixtures (*e.g.*, those with EGaIn : $C_{20}H_{42}$ volume ratios of 3 : 7–1 : 9; Fig. 1b, right) revealed no evidence of such bulk LM envelopment. Instead, only fragmented aggregates ranging in size from tens to hundreds of micrometers were observed. With excess $C_{20}H_{42}$, EGaIn likely lacked sufficient surface area to cover all the $C_{20}H_{42}$ particles, leading to its confinement within the surrounding $C_{20}H_{42}$ particles. Under higher magnification in SEM imaging of these aggregates, severe charging

Open Access Article. Published on 17 November 2025. Downloaded on 3/3/2026 11:12:49 AM. This article is licensed under a Creative Commons Attribution 3.0 Unported Licence.

phenomena were observed, indicating that the organic $C_{20}H_{42}$ primarily covered the surface of metallic EGaIn (data not shown). In the XRD patterns of these $C_{20}H_{42}$-rich mixtures, numerous sharp peaks corresponding to crystalline $C_{20}H_{42}$ appeared prominently along with the broad peak of bulk LM, indicating the presence of $C_{20}H_{42}$ that was not enveloped by bulk LM. It should be noted, however, that no entirely new crystalline peaks unrelated to $C_{20}H_{42}$ were detected.

The attenuated total reflectance-Fourier transform infrared (ATR-FTIR) spectra of the EGaIn–$C_{20}H_{42}$ mixtures (Fig. 1d) generally exhibited higher absorbance than that of pure $C_{20}H_{42}$, which can be attributed to the enhanced interaction with IR electromagnetic radiation induced by the presence of EGaIn.[42] For pure EGaIn and EGaIn-rich mixtures, as is often the case with bulk metals, the signal-to-noise ratio was excessively low, rendering meaningful spectral analysis infeasible. Fig. 1d shows the spectra of an EGaIn : $C_{20}H_{42}$ mixture with a volume ratio of 2 : 8, which had transformed into a black solid powder, as a representative example of $C_{20}H_{42}$-rich composites, compared with that of pure $C_{20}H_{42}$. Notably, both pure $C_{20}H_{42}$ and the hybrid displayed similar characteristic bands: ~2900 cm^{-1}, ~1460 cm^{-1}, and ~690 cm^{-1}, corresponding to the C–H stretching, scissoring, and rocking vibrations of paraffin, respectively.[43] Importantly, no significant evidence was observed for new functional groups—such as carboxylic acids—that could form *via* potential metal-catalyzed oxidation reactions,[44] indicating the chemical stability of paraffinic $C_{20}H_{42}$. The differential scanning calorimetry (DSC) curves of the mixtures, recorded over a wide temperature range (−150 °C to 100 °C), typically exhibited two completely distinct peaks corresponding to the bulk phase-change behaviors of the respective components during both heating and cooling (Fig. S1), indicating that the two materials coexist as separate phases rather than forming a new one.

The blended mixtures remained macroscopically stable without visible phase separation under ambient conditions, maintaining their morphological integrity over extended periods (>1 year; Fig. S2). The adhesion between the chemically dissimilar LM and paraffin phases is likely achieved through the thin oxide "skin" formed on the LM surface.[45,46] While it is theoretically difficult for a non-reactive dielectric material to achieve strong adhesion with a bare LM surface because of the extremely high surface energy of LM,[47,48] many previous studies have demonstrated that the low-surface-energy oxide layer on LM surface significantly enhances its interfacial adhesion with various materials.[40,49] Adopting the widely used Owens–Wendt–Rabel–Kaelble (OWRK) method based on Fowke's classical surface thermodynamic theory,[50–52] we calculated the work of adhesion between the LM surface oxide and paraffin ($W_{oxide–paraffin}$; see SI). The calculated $W_{oxide–paraffin}$ of −74.2 mJ m^{-2} is lower but on the same order of magnitude as the work of adhesion between two LM oxide surfaces ($W_{oxide–oxide} = -131.4$ mJ m^{-2}), both of which are markedly smaller in magnitude than that between oxide-free, pristine LM–LM interfaces ($W_{LM–LM} = -2\gamma_{LM} < 1200$ mJ m^{-2}).[47,52] This comparison suggests that when an oxide layer is present, adhesion between the LM and paraffin phases—through the replacement of oxide–oxide contacts by oxide–paraffin interfaces—becomes energetically much more viable than the hypothetical replacement of pristine LM–LM contacts with LM–paraffin interfaces. In a realistic scenario, the LM–paraffin interface likely forms a composite interfacial region consisting of both the surface oxide and exposed bare LM generated during the mixing process.[45] Unfortunately, direct observation of the interfacial structure *via* electron microscopy at higher magnification was limited due to the rapid melting of paraffins under beam irradiation.

The mixtures were emulsified by combining them with a 20 wt% polyvinyl alcohol (PVA) aqueous solution at a 5 : 5 volume ratio, using a mortar and pestle. This process dispersed the mixtures into small particles within an aqueous continuous phase. Images of selected compositions observed using a transmitted light microscope equipped with a polarizing filter are presented in Fig. 2. Pure EGaIn particles appeared uniformly dark because the light irradiated from beneath the sample cannot transmit through them (Fig. S3a). In contrast, pure $C_{20}H_{42}$ particles exhibited a lustrous appearance owing to their high crystallinity (Fig. S3b). Examination of the hybrid particles of EGaIn and $C_{20}H_{42}$ reveals distinct morphological characteristics depending on their composition. For EGaIn-rich compositions, such as volume ratios of 9 : 1 and 7 : 3, $C_{20}H_{42}$ was scarcely observed, as most of it was encapsulated within LM droplets. The SEM image of the 7 : 3 composition in Fig. 3a shows dispersed particles with relatively smooth surfaces, resembling those observed on pure LM droplets. Energy dispersive X-ray spectroscopy (EDS) analysis in Fig. 3b confirms these surfaces as LM. These surfaces occasionally exhibited cracks, with $C_{20}H_{42}$ protruding from within the LM droplets, though such instances were rare. As the $C_{20}H_{42}$ content increased, the surface cracks became more pronounced, and more $C_{20}H_{42}$ extruded from the LM droplets, with the interior of the droplets becoming saturated with $C_{20}H_{42}$. Starting from the 5 : 5 composition, where the precursor mixtures exhibited a wet sand-like texture, the hybrid particles with surfaces covered by irregularly shaped $C_{20}H_{42}$ clusters increased significantly. This trend became more pronounced at higher $C_{20}H_{42}$ proportions, such as in the 4 : 6 and 3 : 7 compositions, with the SEM/EDS analysis for the latter shown in Fig. 3c. Accordingly, the polarized light microscopy (Fig. 2) revealed a progressively increasing lustrous substance, attributed to $C_{20}H_{42}$, surrounding the EGaIn droplets in $C_{20}H_{42}$-rich compositions. In compositions with extremely high $C_{20}H_{42}$ content, such as 1 : 9, a substantial quantity of individually dispersed $C_{20}H_{42}$ particles was also observed.

Fig. 4 presents the DSC curves for EGaIn–$C_{20}H_{42}$ hybrid particles with various compositions. During heating, all samples exhibited pronounced endothermic peaks at approximately 37–39 °C. During cooling, on the other hand, all samples exhibited pronounced exothermic peaks at approximately 31–33 °C. The temperatures at which these endothermic and exothermic peaks appeared correspond to the melting and crystallization temperatures of bulk $C_{20}H_{42}$, respectively. Thus, these peaks observed in the EGaIn–$C_{20}H_{42}$ hybrid particles likely reflect the solid–liquid phase transition of $C_{20}H_{42}$ within the hybrid particles. The DSC results reveal several

 This journal is © The Royal Society of Chemistry 2026

Open Access Article. Published on 17 November 2025. Downloaded on 3/3/2026 11:12:49 AM.
This article is licensed under a Creative Commons Attribution 3.0 Unported Licence.

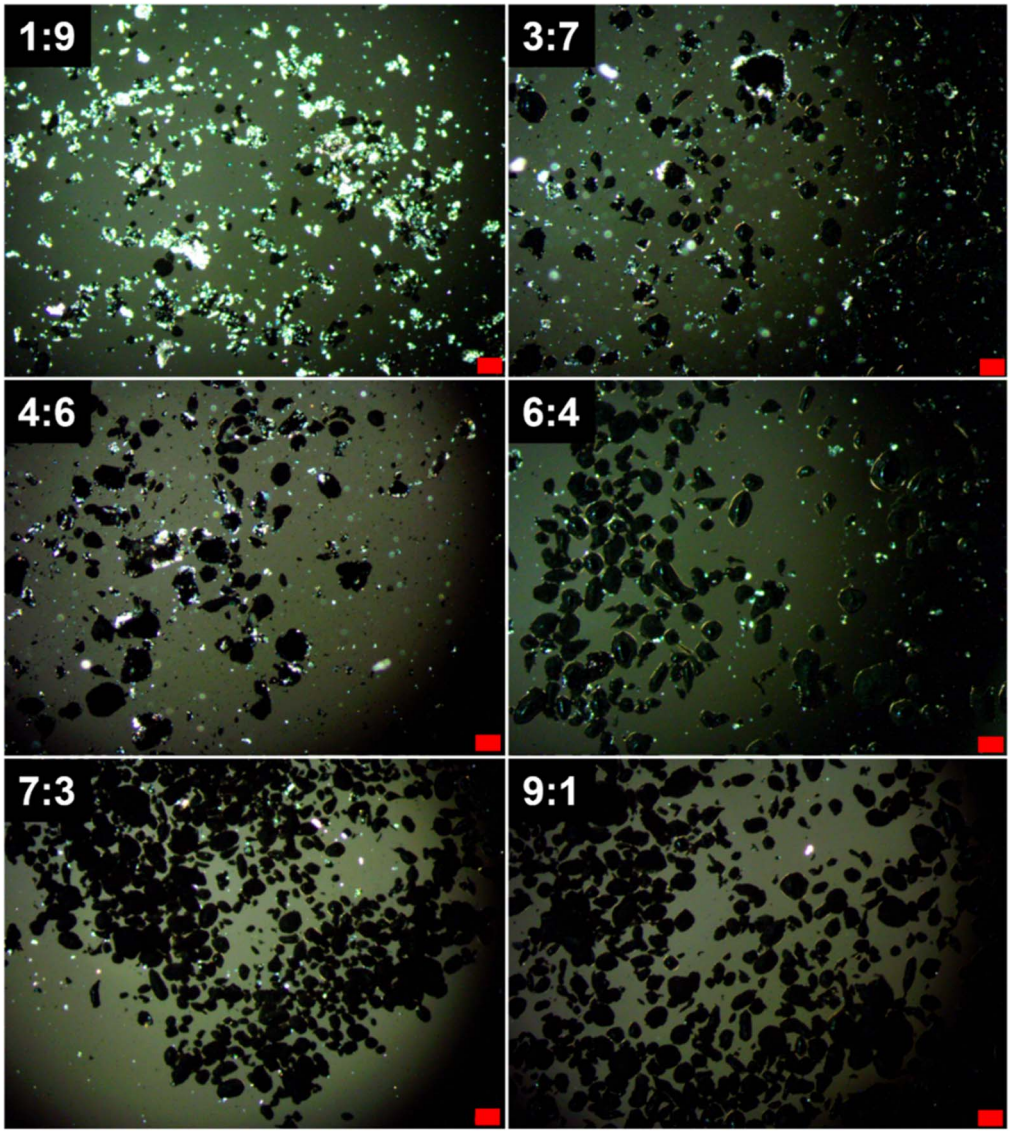

Fig. 2 Polarized light microscopy images of the EGaIn–$C_{20}H_{42}$ hybrid particles at selected EGaIn : $C_{20}H_{42}$ volume ratios (scale bars: 100 μm).

characteristics of these hybrid particles: (1) In EGaIn-rich hybrids, $C_{20}H_{42}$ particles, which were mostly encapsulated within the EGaIn droplets and thus not discernible through polarized light microscopy or SEM, were still present in the hybrids. (2) The melting and crystallization enthalpy values obtained by integrating the DSC curves (Table 1) match the theoretical values calculated based on the compositions of the input materials. This indicates that there was no major loss of $C_{20}H_{42}$ due to its chemical reactions or other processes during the mixing of EGaIn and $C_{20}H_{42}$. (3) As the $C_{20}H_{42}$ content in the hybrid increased, both the melting (ΔH_m) and crystallization (ΔH_c) enthalpy values systematically increased. For example, in the EGaIn-rich composition with an EGaIn : $C_{20}H_{42}$ ratio of 7 : 3, $\Delta H_m = 15.2$ J g^{-1} and $\Delta H_c = 14.7$ J g^{-1}, while in the $C_{20}H_{42}$-rich composition with an EGaIn : $C_{20}H_{42}$ ratio of 2 : 8, $\Delta H_m = 57.4$ J g^{-1} and $\Delta H_c = 57.8$ J g^{-1}. This demonstrates that the latent heat storage and release capacities of the hybrids increased during heating and cooling processes, respectively, with higher $C_{20}H_{42}$ proportions.

Simulated sunlight with an intensity of 1 SUN (1 kW m^{-2}) was irradiated onto surfaces coated with hybrid particles of varying EGaIn-to-$C_{20}H_{42}$ ratios (Fig. 5a), and the resulting temperature changes on the surface were observed using an IR camera (Fig. 5b). The temperatures at three different points on the surface (spot 1, 2, and 3, corresponding to the middle, left, and right points, respectively) were measured simultaneously, and no significant differences were found among the measurements (Fig. S5). Fig. 5c shows the average temperatures of the three points as functions of time. The temperature at the point outside the hybrid particle-coated surfaces (spot 4), exposed to the same simulated sunlight, did not increase significantly (Fig. S5). Similarly, surfaces coated solely with $C_{20}H_{42}$ particles (*i.e.*, EGaIn : $C_{20}H_{42}$ volume ratio = 0 : 10) exhibited only a minor temperature increase (Fig. S6). On the

Open Access Article. Published on 17 November 2025. Downloaded on 3/3/2026 11:12:49 AM.
This article is licensed under a Creative Commons Attribution 3.0 Unported Licence.

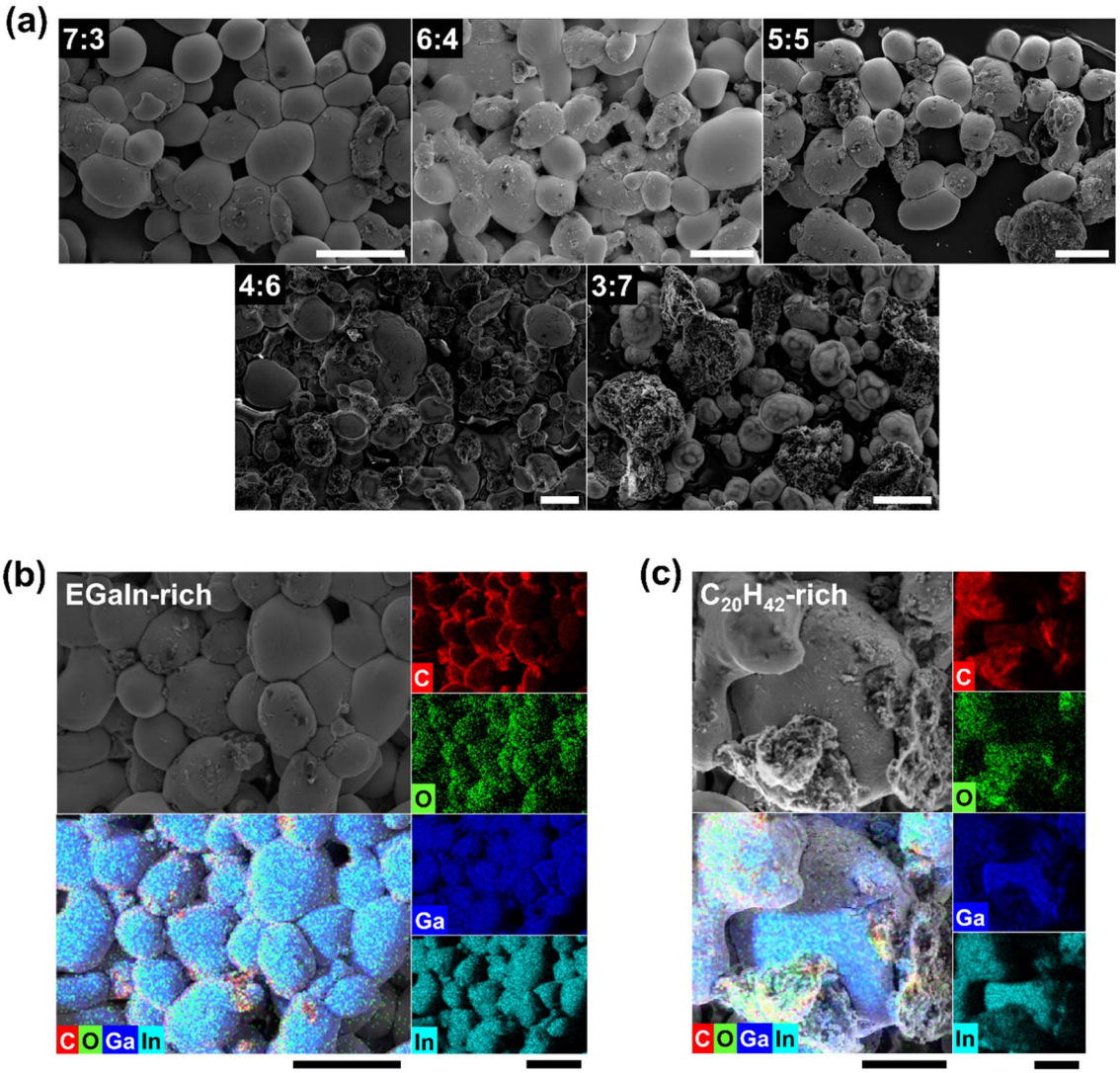

Fig. 3 (a) SEM images of the EGaIn–$C_{20}H_{42}$ hybrid particles at selected EGaIn : $C_{20}H_{42}$ volume ratios (scale bars: 100 μm). SEM/EDS analysis of the hybrid particles with (b) EGaIn-rich (7 : 3) and (c) $C_{20}H_{42}$-rich (3 : 7) compositions (scale bars in b: 100 μm; scale bars in c: 50 μm).

other hand, all surfaces containing EGaIn exhibited a rapid temperature rise within one minute, attributed to the high photothermal conversion properties of EGaIn.

There were two main interesting observations regarding the temperature change behavior of surfaces containing both EGaIn and $C_{20}H_{42}$. First, after a rapid initial rise in surface temperature, a plateau region occurred where the temperature remained steady for several minutes, between 33 °C and 37 °C. The delay in temperature increase during this region was likely due to the phase transition of $C_{20}H_{42}$ from solid to liquid, where it absorbed the heat generated by the photothermal conversion of EGaIn in the form of latent heat. The DSC results shown in Fig. 4 indicated similar endothermic behavior for these hybrids in the same temperature range. This plateau region eventually ended, probably due to the completion of the phase transition of $C_{20}H_{42}$. Afterward, the surface temperature began to rise again, driven by the continued photothermal conversion of EGaIn, with the rate gradually decreasing as the system approached equilibrium. When the simulated sunlight was turned off after 20 minutes, a sharp decrease in temperature from the maximum temperature was observed. Interestingly, plateau regions appeared once again between 34 and 36 °C. The delay in the temperature drop during this region was likely due to the phase transition of $C_{20}H_{42}$ from liquid to solid, which released the latent heat absorbed during heating, as inferred from the exothermic behavior of these hybrids observed in DSC near this temperature range. As the amount of $C_{20}H_{42}$ in the hybrid particles increased, the duration of the plateau region became longer, and the time required for the surface to cool to room temperature also increased. This is because, with more $C_{20}H_{42}$, a greater amount of the stored latent heat could be released, hindering the cooling of the surface. These observed latent heat effects suggest that the EGaIn–$C_{20}H_{42}$ hybrids can be used to store solar energy in the form of latent heat near the phase transition temperature of the PCM, $C_{20}H_{42}$, and release it for use when needed.

Apart from these latent heat effects, another significant effect of $C_{20}H_{42}$ is its ability to greatly enhance the overall

 This journal is © The Royal Society of Chemistry 2026

Open Access Article. Published on 17 November 2025. Downloaded on 3/3/2026 11:12:49 AM.
This article is licensed under a Creative Commons Attribution 3.0 Unported Licence.

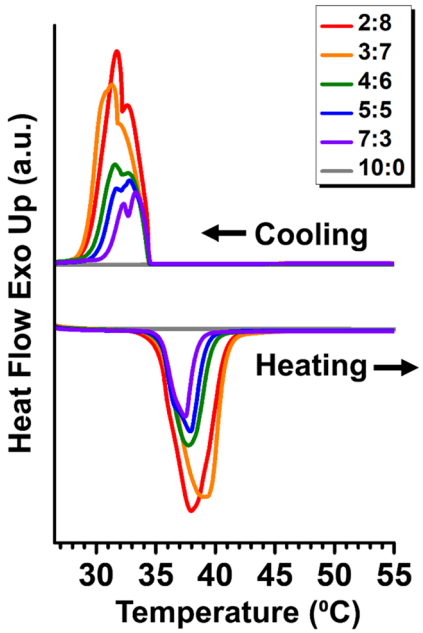

Fig. 4 DSC heating and cooling curves of the EGaIn–$C_{20}H_{42}$ hybrid particles at selected EGaIn : $C_{20}H_{42}$ volume ratios. Baseline corrections were applied to all overlapping data, and normalization was performed with respect to the maximum heat flow peak.

Table 1 Experimental melting (ΔH_m) and crystallization (ΔH_c) enthalpies, and theoretical enthalpy (ΔH_t)[a]

EGaIn : $C_{20}H_{42}$	ΔH_m (in J g^{-1})	ΔH_c (in J g^{-1})	ΔH_t (in J g^{-1})[1]
7 : 3	15.16	14.7	9.69
5 : 5	23.31	22.69	20.91
4 : 6	29.42	29.62	29.43
3 : 7	54.75	54.50	41.51
2 : 8	57.36	57.75	59.97

[a] The ΔH_t values were estimated by multiplying the mass fraction of $C_{20}H_{42}$ in each hybrid formulation by the average enthalpy of 199.7 J g^{-1}, corresponding to the solid–liquid transition of bulk $C_{20}H_{42}$. The discrepancies observed between the experimental and theoretical enthalpy values for certain compositions are most likely attributed to sample inhomogeneity during the DSC measurements, which may have resulted from the very small sample mass (<5 mg) used in the analysis. Nevertheless, the overall trend remains consistent with the theoretical expectations. The agreement between the experimental and theoretical enthalpy values for the EGaIn–$C_{20}H_{42}$ hybrid particles at selected compositions was further verified using a different $C_{20}H_{42}$ product that exhibited slightly higher bulk enthalpy and altered phase-change kinetics (Fig. S4).

temperature rise of surfaces coated with hybrid particles, *i.e.*, the sensible heat effect. As shown in Fig. 5c, it is evident that increasing the $C_{20}H_{42}$ content within the hybrid particles led to a greater surface temperature rise, despite the corresponding reduction in the amount of EGaIn, which served as the photothermal agent. When $C_{20}H_{42}$ was entirely absent, the temperature rise was the lowest, with a final temperature of 33.65 °C after 20 minutes of simulated solar irradiation; the temperature change (ΔT) from the initial temperature in this case was merely ~7 °C. This low solar-to-thermal conversion efficiency aligns with previous studies reporting similar results for pure EGaIn microdroplets.[52] We also dispersed EGaIn *via* ultrasonication to achieve particles approximately 1 μm or smaller in size—orders of magnitude smaller, and invisible under optical microscopy (as shown in Fig. S7a). The surfaces were then coated with these ultrasonically dispersed particles, and their temperature changes under the same intensity of simulated solar irradiation were measured. The results (Fig. S7b) similarly demonstrated a low temperature rise, indicating that particle size was not a critical factor in the poor solar-to-thermal conversion efficiency of pure EGaIn droplets. On the other hand, when $C_{20}H_{42}$ was present, the initial 1 minute period, during which the surface temperature rose sharply before reaching the plateau associated with $C_{20}H_{42}$'s phase transition, showed an increased rate of temperature rise as the $C_{20}H_{42}$ content increased. After surpassing the plateau and undergoing additional temperature increases, the final temperatures for each surface were observed to be 37.4, 39.8, 41.4, 43.0, and 45.9 °C for EGaIn : $C_{20}H_{42}$ ratios of 7 : 3, 5 : 5, 4 : 6, 3 : 7, and 2 : 8, respectively; the corresponding ΔT values were 11.4, 13.8, 15.4, 17.0, and 19.9 °C, respectively. The steady-state photothermal conversion efficiencies (η) of each system were calculated (SI), and the results are presented in Fig. 5d. For the EGaIn-only particles without $C_{20}H_{42}$, η was approximately 34.5%. The blending with paraffin was found to systematically enhance this value, yielding a maximum η of 83.3% at an EGaIn : $C_{20}H_{20}$ ratio of 2 : 8. This value falls within the range previously reported for LM-based photothermal systems that were either chemically modified or coupled with external light absorbers (Table S2).[5,13,25–28] This finding suggests that broadband solar harvesting by EGaIn does not necessarily require complex chemical processing, providing useful insights for the rational design of future LM-based solar-harvesting system. The η values observed for the 2 : 8 composition and other hybrid ratios are also comparable to, or in some cases even exceed, those reported for many metallic, semiconductor, carbon-based, and polymeric photothermal materials.[1] Contrary to common perception, these results demonstrate that LMs can serve as highly effective solar-harvesting materials, even through simple physical blending without the need for elaborate chemical modification.

The reason why EGaIn demonstrated higher solar-to-thermal conversion efficiency when blended with $C_{20}H_{42}$ is worth discussing. $C_{20}H_{42}$ is an organic compound composed solely of sigma bonds, and it exhibits relatively low broadband absorption in the UV-visible range.[53] It has been shown to have limited photothermal conversion capability under simulated solar irradiation on its own (Fig. S6). $C_{20}H_{42}$ is a chemically stable compound, and the likelihood of forming new bulk compounds upon mixing with EGaIn is low. As shown in Fig. 1c and d, there was little evidence of new compound formation in the precursor mixture of the $C_{20}H_{42}$-rich hybrid, where a pronounced photothermal conversion effect was observed. Moreover, as demonstrated in Fig. 4 and Table 1, the latent heat absorption and release of the EGaIn-$C_{20}H_{42}$ hybrid particles closely matched the amount of $C_{20}H_{42}$ introduced, indicating that no major chemical reactions occurred that could lead to significant consumption of $C_{20}H_{42}$. Thus, the mechanism underlying the enhanced solar-to-

Open Access Article. Published on 17 November 2025. Downloaded on 3/3/2026 11:12:49 AM.
This article is licensed under a Creative Commons Attribution 3.0 Unported Licence.

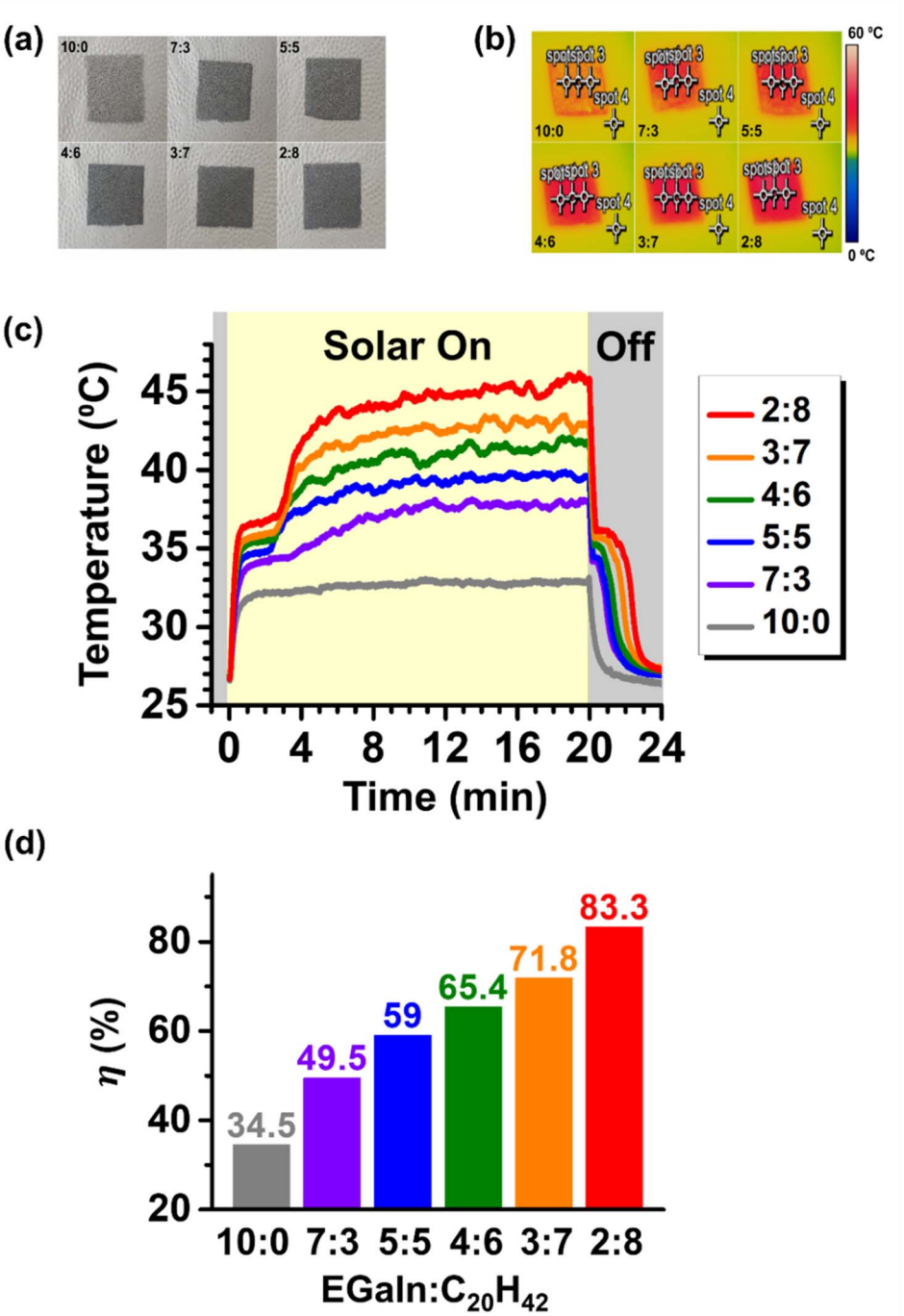

Fig. 5 (a) Photographs of surfaces coated with EGaIn–$C_{20}H_{42}$ hybrid particles with various EaIn : $C_{20}H_{42}$ volume ratios, and (b) their IR images captured after 20 minutes of simulated solar irradiation (1 kW m^{-2}). (c) Average temperatures of three points on the hybrid-coated surfaces with various EaIn : $C_{20}H_{42}$ volume ratios, represented as functions of time (solar on: 0–20 min; solar off: 20–24 min). (d) Calculated steady-state photothermal conversion efficiencies (η).

thermal conversion is more appropriately explored by probing the local interfacial changes between EGaIn and $C_{20}H_{42}$.

Using density functional theory (DFT) simulations, we investigated the adsorption of a $C_{20}H_{42}$ molecule on the (100) surface of hexagonal EGaIn bulk (Fig. 6a), identified as the most energetically favored facet (Fig. S8). The adsorption energy per $C_{20}H_{42}$ molecule was calculated to be $E_{ad} = -0.42$ eV, indicating that the adsorption is essentially physisorption.

Partial density of states (PDOS) calculations for the EGaIn–$C_{20}H_{42}$ interface revealed that the metallic character required for plasmonic response is preserved (Fig. 6b). Interestingly, this physisorption shifted the Fermi energy level (E_f) from −1.14 eV to −2.24 eV (Fig. 6c). This strongly suggests that the adsorbed paraffin, although generally regarded as nonpolar, can induce electron redistribution and form interfacial dipoles. Notably, the

 This journal is © The Royal Society of Chemistry 2026

Open Access Article. Published on 17 November 2025. Downloaded on 3/3/2026 11:12:49 AM.
This article is licensed under a Creative Commons Attribution 3.0 Unported Licence.

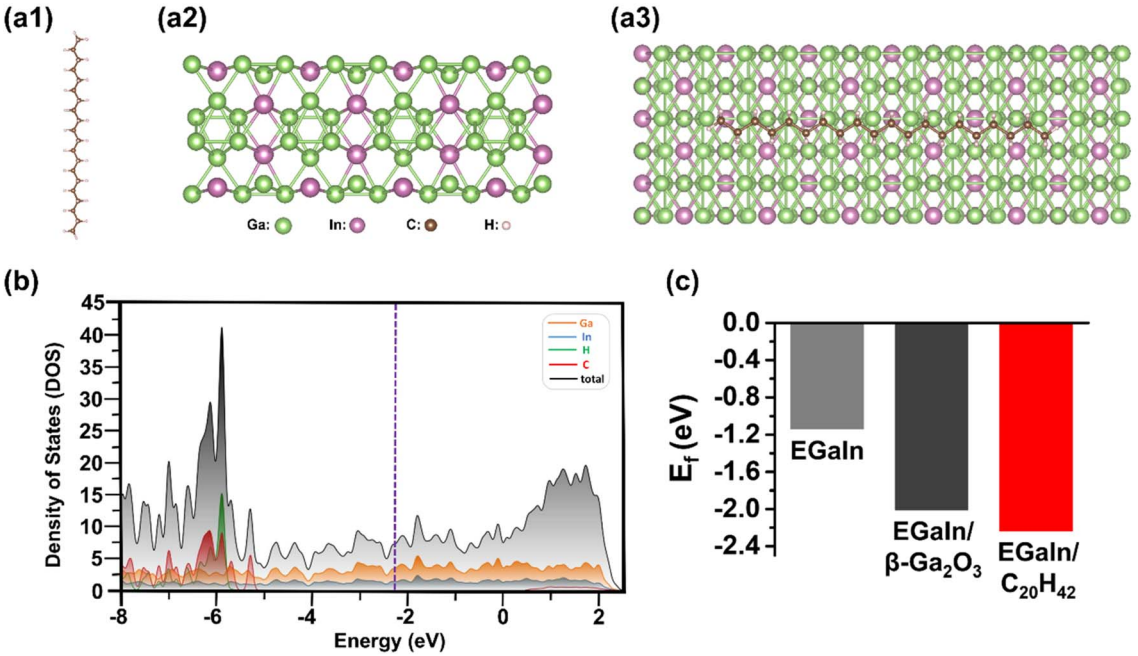

Fig. 6 DFT optimized geometries of (a1) $C_{20}H_{42}$ and (a2) the (100) hexagonal EGaIn surface, and (a3) $C_{20}H_{42}$-adsorbed EGaIn surface at its most favorable configuration. (b) Density of states (DOS) of the EGaIn–$C_{20}H_{42}$ hybrid, where the dotted vertical line (purple color) represents the Fermi energy level ($E_f = -2.24$ eV). (c) Calculated E_f values for different interfacial compositions.

calculated E_f was even lower than that of the EGaIn–Ga_2O_3 interface, which may be present on native EGaIn surfaces (Fig. S9).

The ATR-FTIR spectra of the hybrid particles, emulsified and collected in aqueous PVA solution for the photothermal conversion experiments, were dominated by signals from the functional groups of adsorbed PVA on the particle surfaces (Fig. S10), which limited the ability to accurately assess interfacial changes arising from compositional differences. However, a detailed investigation using X-ray photoelectron spectroscopy (XPS) enabled the detection of subtle interfacial variations in the hybrid particles depending on the blending ratio. Fig. 7 and 8 present the surface narrow-scan spectra and depth profiling results for the C and Ga elements in pure EGaIn, EGaIn-rich hybrid, and $C_{20}H_{42}$-rich hybrid particles. The C 1s narrow-scan spectra (Fig. 7a–c) showed that the hybrid particles blended with $C_{20}H_{42}$ exhibited a relatively stronger C–C peak

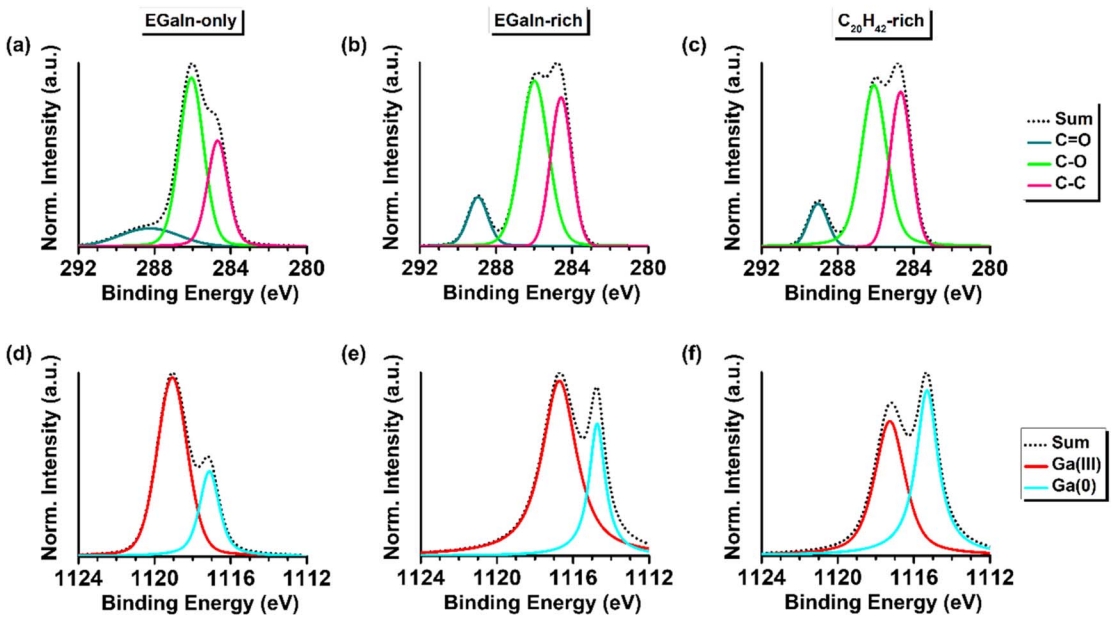

Fig. 7 XPS (a–c) C 1s and (d–f) Ga 2p narrow scan spectra for the surfaces coated with pure EGaIn (EGaIn : $C_{20}H_{42}$ = 10 : 0; a and d), EGaIn-rich hybrid (EGaIn : $C_{20}H_{42}$ = 7 : 3; b and e), and $C_{20}H_{42}$-rich hybrid (EGaIn : $C_{20}H_{42}$ = 3 : 7; c and f) particles.

Open Access Article. Published on 17 November 2025. Downloaded on 3/3/2026 11:12:49 AM.
This article is licensed under a Creative Commons Attribution 3.0 Unported Licence.

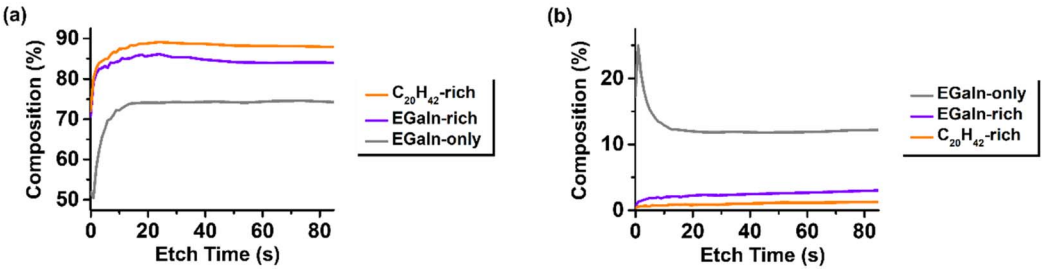

Fig. 8 Depth profiling analysis of the surfaces coated with pure EGaIn (EGaIn : $C_{20}H_{42}$ = 10 : 0), EGaIn-rich hybrid (EGaIn : $C_{20}H_{42}$ = 7 : 3), and $C_{20}H_{42}$-rich hybrid (EGaIn : $C_{20}H_{42}$ = 3 : 7) particles. Atomic compositions (%) of (a) C and (b) Ga elements are shown as functions of etch time.

compared to the EGaIn-only particles, which was attributed to the sp^3 carbons of the surface-adsorbed paraffin $C_{20}H_{42}$. Depth profiling analysis further suggested that the hybrid particles possessed a much higher carbon content at and beneath the surface than the EGaIn-only particles, and that the $C_{20}H_{42}$-rich particles contained more surface carbon than the EGaIn-rich particles (Fig. 8). This indicated that hybridized $C_{20}H_{42}$ formed a substantially thicker dielectric layer on the surface of the EGaIn droplets. Interestingly, for the EGaIn-only particles, the C═O peak among the PVA-derived C–O and C═O signals was significantly reduced (Fig. 7a), which could be attributed to the consumption of residual acetyl groups of PVA through reactions with the metal surface. In contrast, for the hybrid particles, the thick $C_{20}H_{42}$ layer covering the EGaIn surface was presumed to suppress such reactions between the reactive PVA functional groups and the EGaIn surface (Fig. 7b and c). Related to this, the Ga 2p narrow-scan spectra (Fig. 7d–e) showed that, as the $C_{20}H_{42}$ content increased, the surface Ga oxide (Ga(III)) decreased while the metallic Ga (Ga(0)) increased, suggesting that the $C_{20}H_{42}$ covering partially mitigated surface oxidation. Collectively, the hybridized $C_{20}H_{42}$ forms a thick dielectric layer on the EGaIn droplet surfaces, which does not undergo bulk chemical reactions but rather mitigates potential reactions of the EGaIn surface with other materials.

Fig. 9 shows the relative reflectance of surfaces coated with the hybrid particles measured across the UV-visible-NIR wavelength range (250–2500 nm), corresponding to the solar spectrum. As the $C_{20}H_{42}$ content in the hybrid composition increased, the direct surface reflectance decreased systematically across the entire wavelength range, indicating that a higher $C_{20}H_{42}$ content led to greater absorption of incident electromagnetic radiation. The broadband decrease in reflectance is most reasonably understood as the collective result of several mutually coupled effects.[54] First, the paraffin layer encapsulating the metallic

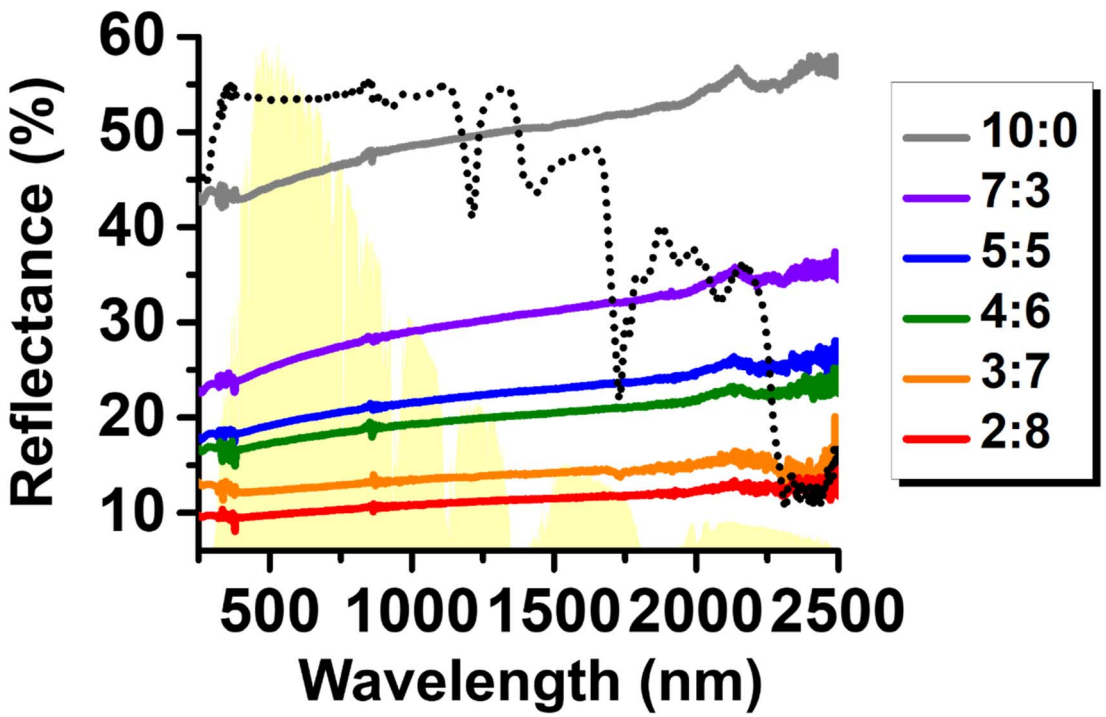

Fig. 9 Relative reflectance of broadband light (250–2500 nm) by the hybrid-coated surfaces with various EaIn : $C_{20}H_{42}$ volume ratios. The dotted black line corresponds to the surface coated with $C_{20}H_{42}$-only (0 : 10) particles. The yellow shading represents the AM 1.5G solar spectrum.

 This journal is © The Royal Society of Chemistry 2026

Open Access Article. Published on 17 November 2025. Downloaded on 3/3/2026 11:12:49 AM. This article is licensed under a Creative Commons Attribution 3.0 Unported Licence.

droplets establishes a metal–dielectric–air optical boundary that suppresses specular reflection and enhances near-field coupling. This dielectric interface increases the local optical path length and facilitates photon–metal interaction, improving energy dissipation through plasmonic thermalization.[55] Second, pronounced micro-*meso*-scale surface roughness, as revealed for paraffin-rich hybrids in SEM and optical micrographs, may disrupt mirror-like reflection and induce multiple internal bounces before re-emission. Such texturing is known to increase effective absorption even when the dielectric itself is only weakly absorbing, owing to geometric light-trapping effects.[56] Finally, at high paraffin loadings, spatially separated EGaIn domains embedded in semi-transparent wax likely promote interparticle scattering and reabsorption, further extending the photon residence time within the composite. Notably, when surfaces were coated with $C_{20}H_{42}$-only particles and their reflectance was measured (Fig. 9), $C_{20}H_{42}$ exhibited very high reflectance in the UV-visible region. Nevertheless, increasing its fraction within the hybrid particles led to a more pronounced reduction of reflectance (or equivalently, stronger absorption) in the UV-visible region than in the infrared region. This trend supports the interpretation that the wax domains located on and between the LM droplets induce multiple scattering of incident light, particularly at shorter wavelengths, thereby effectively suppressing direct reflection and promoting diffuse reabsorption within the hybrid particle assemblies. Although these effects are difficult to deconvolute quantitatively within the present study, their combined influence provides a consistent physical picture for the experimentally observed reduction in broadband reflectance and the accompanying enhancement in photothermal heating.

Ultimately, a significant reduction in the proportion of the costly and heavy photothermal agent EGaIn led to a higher temperature rise effect when hybridized with $C_{20}H_{42}$. Together with the latent heat effects discussed earlier, it can be concluded that increasing the $C_{20}H_{42}$ proportion in the EGaIn-$C_{20}H_{42}$ hybrid particles for solar-to-thermal conversion systems could lead to both greater sensible heat effects and enhanced latent heat utilization, featuring the unique potential of the proposed blending approach for EGaIn-mediated solar energy harvesting. As a final technical note, we would like to clarify that the hybrids presented in this study were designed as model systems for fundamental investigation of thermal effects, rather than as ready-to-use materials. For more practical applications, the hybrids should be appropriately encapsulated to prevent leakage of liquefied $C_{20}H_{42}$ during operation. This can be readily achieved by dispersing the hybrid particles as "fillers" within suitable base polymer matrices tailored to specific applications such as solar water harvesting[30,31] or passive thermal management.[32] The polymer matrices employed for this purpose should ideally possess minimal porosity to securely retain the liquefied $C_{20}H_{42}$, while exhibiting low reflectance toward broadband solar light so that the embedded hybrids can effectively absorb incident radiation.

Conclusion

In this study, we reported the enhanced photothermal conversion efficiency of LM EGaIn under broadband solar irradiation when hybridized with the paraffin wax $C_{20}H_{42}$. On its own, $C_{20}H_{42}$ exhibited low solar absorption and did not contribute to photothermal conversion. Moreover, as a chemically stable compound, $C_{20}H_{42}$ did not react with EGaIn to form new bulk compounds. When blended with EGaIn to form a precursor mixture, which was then dispersed as colloidal particles, $C_{20}H_{42}$ was either encapsulated within the resulting EGaIn droplets or covered their exteriors. The latter formed a thick dielectric layer and significantly lowered the direct reflectance of the EGaIn surfaces over a broad wavelength range, thereby markedly enhancing photothermal heating effects under simulated solar irradiation. Under simulated sunlight at an intensity of 1 SUN for 20 minutes, the final ΔT of a surface coated with pure EGaIn droplets was only ~7 °C, whereas that of an EGaIn–$C_{20}H_{42}$ hybrid with a EGaIn : $C_{20}H_{42}$ volume ratio of 2 : 8 reached 19.9 °C. The calculated photothermal conversion efficiency of 83.3% for the hybrid system falls within the range reported for high-performance LM-based solar-to-thermal conversion materials. Notably, this high efficiency was achieved through a simple physical blending process, without any irreversible or complex chemical reactions or the incorporation of strongly light-absorbing additives. When the hybrid-coated surface was heated by sunlight or cooled by removing sunlight, temperature plateaus were observed within the range of approximately 33–37 °C for several minutes. This phenomenon arose from the PCM characteristics inherent to $C_{20}H_{42}$. $C_{20}H_{42}$ underwent solid–liquid phase transitions within this temperature range, absorbing (when transitioning from solid to liquid upon heating) or releasing (when transitioning from liquid to solid upon cooling) latent heat. Because chemical reactions between $C_{20}H_{42}$ and EGaIn, which could potentially compromise this property, were unlikely to have occurred, the hybrid materials exhibited latent heat storage and release capacities consistent with theoretical values, depending on the mixing ratios. As the volume fraction of $C_{20}H_{42}$ in the hybrid increased, its latent heat capacities also increased. For instance, in the EGaIn-rich composition of EGaIn : $C_{20}H_{42}$ = 7 : 3, $\Delta H_m = 15.2$ J g^{-1} and $\Delta H_c = 14.7$ J g^{-1}, whereas in the $C_{20}H_{42}$-rich composition of EGaIn : $C_{20}H_{42}$ = 2 : 8, $\Delta H_m = 57.4$ J g^{-1} and $\Delta H_c = 57.8$ J g^{-1}. Consequently, by significantly increasing the proportion of $C_{20}H_{42}$ in the EGaIn–$C_{20}H_{42}$ hybrid, both the sensible heat effect (*i.e.*, higher ΔT) and the latent heat utilization effect (*i.e.*, higher ΔH_m and ΔH_c) can be enhanced. Notably, the former effect is somehow paradoxical, given the significantly reduced proportion of EGaIn–the photothermal agent–in the hybrid composition. The current study proposes a unique conceptual strategy for enhancing EGaIn-mediated solar energy harvesting, addressing both sensible and latent heat effects, by employing non-reactive, non-solar-absorbing paraffin-based PCMs-an approach that sets it apart from previous studies.

Conflicts of interest

There are no conflicts of interest to declare.

Data availability

The data supporting this article have been included as part of the supplementary information (SI). Supplementary

Open Access Article. Published on 17 November 2025. Downloaded on 3/3/2026 11:12:49 AM. This article is licensed under a Creative Commons Attribution 3.0 Unported Licence.

information (SI): experimental details; DSC heating and cooling curves of an EGaIn–$C_{20}H_{42}$ precursor mixture (3 : 7); photographs of the precursor mixtures after long-term storage; polarized light microscopy images of EGaIn (10 : 0) and $C_{20}H_{42}$ (0 : 10) particles; DSC heating and cooling of curves of hybrids at selected EGaIn : $C_{20}H_{42}$ volume ratios using a different $C_{20}H_{42}$ product; temperature variations at three points (spot 1, 2, and 3) on a hybrid (EGaIn : $C_{20}H_{42}$ = 2 : 8)-coated surface and one point (spot 4) outside the coated surface; temperature variations (ΔT) on surfaces coated with $C_{20}H_{42}$-only (0 : 10) particles; SEM image of ultrasonicated EGaIn particles (10 : 0); average temperature of three points on the ultrasonicated EGaIn particle (10 : 0)-coated surface; optimization of the EGaIn and EGaIn–Ga_2O_3 structures and the calculated PDOS in DFT simulations; ATR-FTIR spectra of EGaIn-rich (7 : 3) and $C_{20}H_{42}$-rich (3 : 7) hybrid particles, obtained from PVA-mediated emulsions after water evaporation; calculation methods for work of adhesion and photothermal conversion efficiency. See DOI: https://doi.org/10.1039/d5ta07484c.

Acknowledgements

This work was supported by the National Research Foundation of Korea (NRF) grant funded by the Korea government (MSIT) (RS-2025-16065277, RS-2023-00259994). This research was also supported by Basic Science Research Program through the National Research Foundation of Korea (NRF) funded by the Ministry of Education (RS-2025-25421959, RS-2024-00460455).

References

1 X. Cui, Q. Ruan, X. Zhuo, X. Xia, J. Hu, R. Fu, Y. Li, J. Wang and H. Xu, Photothermal Nanomaterials: A Powerful Light-to-Heat Converter, *Chem. Rev.*, 2023, **123**, 6891–6952.

2 A. M. Pornea and H. Kim, Core-Satellite Assembly of Phase-Changing Material Microcapsules Enabled with Broadband Light Absorption and Localized Surface Plasmonic Resonance for Effective Photothermal Energy Harvesting, *Sol. Energy Mater. Sol. Cells*, 2023, **250**, 112075.

3 X. Luo, B. Hao, H. Xiang, H. Li and Z. Tao, A Novel Phase Change Materials Used for Direct Photothermal Conversion and Efficient Thermal Storage, *Sol. Energy Mater. Sol. Cells*, 2023, **251**, 112142.

4 F. Zhao, X. Zhou, Y. Shi, X. Qian, M. Alexander, X. Zhao, S. Mendez, R. Yang, L. Qu and G. Yu, Highly Efficient Solar Vapour Generation *via* Hierarchically Nanostructured Gels, *Nat. Nanotechnol.*, 2018, **13**, 489–495.

5 Z. Wei, C. Cai, Y. Huang, Y. Wang and Y. Fu, Biomimetic Surface Strategy of Spectrum-Tailored Liquid Metal *via* Blackbody Inspiration for Highly Efficient Solar Steam Generation, Desalination, and Electricity Generation, *Nano Energy*, 2021, **86**, 106138.

6 H. W. Liu, C. J. Chen, H. Wen, R. X. Guo, N. A. Williams, B. D. Wang, F. J. Chen and L. B. Hu, Narrow Bandgap Semiconductor Decorated Wood Membrane for High-Efficiency Solar-Assisted Water Purification, *J. Mater. Chem. A*, 2018, **6**, 18839–18846.

7 C. Lei, W. Guan, Y. Guom, W. Shi, Y. Wang, K. P. Johnston and G. Yu, Polyzwitterionic Hydrogels for Highly Efficient High Salinity Solar Desalination, *Angew. Chem., Int. Ed.*, 2022, **61**, e202208487.

8 L. L. Zhu, M. M. Gao, C. K. N. Peh, X. Q. Wang and G. W. Ho, Self-Contained Monolithic Carbon Sponges for Solar-Driven Interfacial Water Evaporation Distillation and Electricity Generation, *Adv. Energy Mater.*, 2018, **8**, 1702149.

9 L. L. Zhu, T. P. Ding, M. M. Gao, C. K. N. Peh and G. W. Ho, Shape Conformal and Thermal Insulative Organic Solar Absorber Sponge for Photothermal Water Evaporation and Thermoelectric Power Generation, *Adv. Energy Mater.*, 2019, **9**, 1900250.

10 T. Hao, Z. Zhu, H. Yang, Z. He and J. Wang, All-Day Anti-Icing/Deicing Film Based on Combined Photo-Electro-Thermal Conversion, *ACS Appl. Mater. Interfaces*, 2021, **13**, 44948–44955.

11 Z. Zhao, Y. Wang, Z. Wang, X. Cui, G. Liu, Y. Zhang, Y. Zhu, J. Chen, S. Sun, K. Zhang, X. Liu and H. Chen, A New Composite Material with Energy Storage, Electro/Photo-Thermal and Robust Super-Hydrophobic Properties for High-Efficiency Anti-Icing/De-Icing, *Small*, 2024, **20**, 2311435.

12 W. Zhang, B. S. Naidu, J. Z. Ou, A. P. O'Mullane, A. F. Chrimes, B. J. Carey, Y. Wang, S.-Y. Tang, V. Sivan, A. Mitchell, S. K. Bhargava and K. Kalantar-Zadeh, Liquid Metal/Metal Oxide Frameworks with Incorporated Ga2O3 for Photocatalysis, *ACS Appl. Mater. Interfaces*, 2015, **7**, 1943–14948.

13 N. Flores, F. Centurion, J. Zheng, M. Baharfar, M. Kilani, M. B. Ghasemian, F.-M. Allioux, J. Tang, J. Tang, K. Kalantar-Zadeh and M. A. Rahim, Polyphenol-Mediated Liquid Metal Composite Architecture for Solar Thermoelectric Generation, *Adv. Mater.*, 2024, **36**, 2308346.

14 B. Yang, C. Li, Z. Wang and Q. Dai, Thermoplasmonics in Solar Energy Conversion: Materials, Nanostructured Designs, and Applications, *Adv. Mater.*, 2022, **34**, 2107351.

15 W. W. Gartner, Photothermal Effect in Semiconductors, *Phys. Rev.*, 1961, **122**, 419–424.

16 T. Daeneke, K. Khoshmanesh, N. Mahmood, I. A. de Castro, D. Esrafilzadeh, S. J. Barrow, M. D. Dickey and K. Kalantar-Zadeh, Liquid Metals: Fundamentals and Applications in Chemistry, *Chem. Soc. Rev.*, 2018, **47**, 4073–4111.

17 S. A. Chechetka, Y. Yu, X. Zhen, M. Pramanik, K. Pu and E. Miyako, Light-Driven Liquid Metal Nanotransformers for Biomedical Theranostics, *Nat. Commun.*, 2017, **8**, 15432.

18 P. Zhu, S. Gao, H. Lin, X. Lu, B. Yang, L. Zhang, Y. Chen and J. Shi, Inorganic Nanoshell-Stabilized Liquid Metal for Targeted Photonanomedicine in NIR-II Biowindow, *Nano Lett.*, 2019, **19**, 2128–2137.

19 N. Xia, N. Li, W. Rao, J. Yu, Q. Wu, L. Tan, H. Li, L. Guo, P. Liang, L. Li and X. Meng, Multifunctional and Flexible Zro_2-Coated EGaIn Nanoparticles for Photothermal Therapy, *Nanoscale*, 2019, **11**, 10183–10189.

20 Y. Lu, Q. Hu, Y. Lin, D. B. Pacardo, C. Wang, W. Sun, F. S. Ligler, M. D. Dickey and Z. Gu, Transformable Liquid-Metal Nanomedicine, *Nat. Commun.*, 2015, **6**, 10066.

 This journal is © The Royal Society of Chemistry 2026

Open Access Article. Published on 17 November 2025. Downloaded on 3/3/2026 11:12:49 AM. This article is licensed under a Creative Commons Attribution 3.0 Unported Licence.

21 X. Zhu, M. Duan, L. Zhang, J. Zhao, S. Yang, R. Shen, S. Chen, L. Fan and J. Liu, Liquid Metal-Enabled Microspheres with High Drug Loading and Multimodal Imaging for Artery Embolization, *Adv. Funct. Mater.*, 2023, **33**, 2209413.
22 J. Park, H. Lee, E. Na, H. Jo, T. S. Shim, C. B. Kim, H. Kim, G. Yu and J. Lee, Structured Liquid-*in*-Liquid Emulsion Stabilized by Surface-Engineered Liquid Metal Droplets as "Mutant" Pickering Emulsifiers, *ACS Appl. Mater. Interfaces*, 2025, **17**, 9945–9959.
23 L. Wang, R. Lai, M. Zhang and L. Fu, Emerging Liquid Metal Biomaterials: From Design to Application, *Adv. Mater.*, 2022, **34**, 2201956.
24 S. Jamalzadegan, M. Zare, M. J. Dickens, F. Schenk, A. Velayati, M. Yarema, M. D. Dickey and Q. Wei, Shape and Size-Dependent Surface Plasmonic Resonance of Liquid Metal Alloy (EGaIn) Nanoparticles, *Nanoscale*, 2025, **17**, 22819–22833.
25 S. Yang, Y. Zhang, J. Bai, Y. He, X. Zhao and J. Zhang, Integrating Dual-Interfacial Liquid Metal Based Nanodroplet Architectures and Micro-Nanostructured Engineering for High Efficiency Solar Energy Harvesting, *ACS Nano*, 2022, **16**, 15086–15099.
26 S. Yang, H. Zhang, X. Sun, J. Bai and J. Zhang, 3D-Printed Liquid Metal-in-Hydrogel Solar Evaporator: Merging Spectrum-Manipulated Micro-Nano Architecture and Surface Engineering for Solar Desalination, *ACS Nano*, 2024, **18**, 5847–5863.
27 S. Yang, Y. He, J. Bai and J. Zhang, Synergistic Dual-Mechanism Localized Heat Channeling and Spectrum-Taiolored Liquid Metal Hydrogels for Efficient Solar Water Evaporation and Desalination, *Small*, 2023, **19**, 2302526.
28 X. Huang, J. Liu, P. Zhou, G. Su, T. Zhou, X. Zhang and C. Zhang, Ultrarobust Photothermal Materials *via* Dynamic Crosslinking for Solar Harvesting, *Small*, 2022, **18**, 2104048.
29 A. Li, H.-Y. Zhao, X. Lu, Z. Yang, J. Liu, Z.-Z. Yu and X. Li, Liquid Metal-Enhanced Phase-Change Composites for Efficient Solar-Thermal-Electric Energy Conversion, *ACS Appl. Mater. Interfaces*, 2025, **17**, 48763–48772.
30 H. Shan, P. Poredos, H. Qu, X. Yang, M. Zhou, L. Bai, J. Shi, W. Chen, R. Wang and S. C. Tan, Integrating Rooftop Agriculture and Atmospheric Water Harvesting for Water-Food Production Based on Hygroscopic Manganese Complex, *Adv. Func. Mater.*, 2024, **34**, 2402839.
31 H. Shan, Z. Ye, J. Yu, R. Wang and Z. Xu, Improving Solar Water Harvesting *via* Airflow Restructuring Using 3D Vapor Generator, *Device*, 2023, **1**, 100065.
32 P. Poredos, H. Shan, C. Wang, Z. Chen, Z. Shao, F. Deng, H. Liu, J. Yu and R. Wang, Radiative Sky Cooling Thermal Concentration with Cooling Power Exceeding One kW per Square Meter, *Energy Environ. Sci.*, 2024, **17**, 2336–2355.
33 S. Kang, W. Kim, C. Song, Y. Hong, S. Kim, M. Goh, S. K. Chung and J. Lee, Novel Latent Heat Storage Systems Based on Liquid Metal Matrices with Suspended Phase Change Material Microparticles, *ACS Appl. Mater. Interfaces*, 2023, **15**, 36781–36791.
34 H. Akeiber, P. Nejat, M. Z. A. Majid, M. A. Wahid, F. Jomehzadeh, I. Z. Famileh, J. K. Calautit, B. R. Hughes and S. A. Zaki, A Review on Phase Change Material (PCM) for Sustainable Passive Cooling in Building Envelopes, *Renewable Sustainable Energy Rev.*, 2016, **60**, 1470–1497.
35 Y. Su, W. Zhu, M. Tian, Y. Wang, X. Zhang and J. Li, Intelligent Bidirectional Thermal Regulation of Phase Change Material Incorporated in Thermal Protective Clothing, *Appl. Therm. Eng.*, 2020, **174**, 115340.
36 C. Liu, D. Xu, J. Weng, D. Zhou, J. Wang and Q. Huang, Phase Change Materials Application in Battery Thermal Management System: A Review, *Materials*, 2020, **13**, 4622.
37 R. Stropnik and U. Stritih, Increasing the Efficiency of PV Panel with the Use of PCM, *Renewable Energy*, 2016, **97**, 671–679.
38 J. Park, Y. Kim, H. Lee, C. Song, S. Kang, Y. Cho and J. Lee, Pickering-Type Phase Change Capsules for Skin-Temperature-Controllable Sunscreen Formulation, *Polymer*, 2024, **48**, 282–288.
39 Z. Chai, M. Fang and X. Min, Composite Phase-Change Materials for Photo-Thermal Conversion and Energy Storage: A Review, *Nano Energy*, 2024, **124**, 109437.
40 W. Kong, Z. Wang, M. Wang, K. C. Manning, A. Uppal, M. D. Green, R. Y. Wang and K. Rykaczewski, Oxide-Mediated Formation of Chemically Stable Tungsten–Liquid Metal Mixtures for Enhanced Thermal Interfaces, *Adv. Mater.*, 2019, **31**, 1904309.
41 D. Wu, D. Liu, X. Tian, C. Lei, X. Chen, S. Zhang, F. Chen, K. Wu and Q. Fu, A A Universal Mechanochemistry Allows On-Demand Synthesis of Stable and Processable Liquid Metal Composites, *Small Methods*, 2022, **6**, 2200246.
42 S. Kim, C. Song, S. Kim, S. Kang, H. G. Menge, Y. T. Park and J. Lee, Effects of a Liquid Metal Co-Filler on the Properties of Expoy/Binary Filler Composites, *J. Appl. Polym. Sci.*, 2024, **141**, e55134.
43 S. Garcia-Vinuales, C. Rubio, L. Martinez-Izquierdo, B. Zornoza, E. Piera, M. A. Caballero and C. Tellez, Study of Melamine-Formaldehyde/Phase Change Material Microcapsules for the Preparation of Polymer Films by Extrusion, *Membranes*, 2022, **12**, 266.
44 M. V. Kirillova, A. M. Kirillov, M. L. Kuznetsov, J. A. L. Silva, J. J. R. F. Silva and A. J. L. Pombeiro, Alkanes to Carboxylic Acids in Aqueous Medium: Metal-Free and Metal-Promoted Highly Efficient and Mild Conversions, *Chem. Commun.*, 2009, 2353–2355.
45 K. Doudrick, S. Liu, E. M. Mutunga, K. L. Klein, V. Damle, K. K. Varanasi and K. Rykaczewski, Different Shades of Oxide: From Nanoscale Wetting Mechanisms to Contact Printing of Gallium-Based Liquid Metals, *Langmuir*, 2014, **30**, 6867–6877.
46 W. Jung, M. H. Vong, K. Kwon, J. U. Kim, S. J. Kwon, T. Kim and M. D. Dickey, Giant Decrease in Interfacial Energy of Liquid Metals by Native Oxides, *Adv. Mater.*, 2024, **36**, 2406783.
47 S. Handschuh-Wang, Y. Chen, L. Zhu and X. Zhou, Analysis and Transformations of Room-Temperature Liquid Metal Interfaces - A Closer Look through Interfacial Tension, *ChemPhysChem*, 2018, **19**, 1584–1592.

Open Access Article. Published on 17 November 2025. Downloaded on 3/3/2026 11:12:49 AM.
This article is licensed under a Creative Commons Attribution 3.0 Unported Licence.

48 J. N. Israelachvili, *Intermolecular and Surface Forces*, Academic Press, Oxford, 2011.
49 H. Chang, P. Zhang, Y. Cui, Y. Hou, Z. Sun and W. Rao, Recoverable Liquid Metal Paste with Reversible Rheological Characteristic for Electronics Printing, *ACS Appl. Mater. Interfaces*, 2020, **12**, 14125–14135.
50 F. M. Fowkes, Attractive Forces at Interfaces, *Ind. Eng. Chem.*, 1964, **56**, 40–52.
51 D. K. Owens and R. C. Wendt, Estimation of the Surface Free Energy of Polymers, *J. Appl. Polym. Sci.*, 1969, **13**, 1741–1747.
52 S. Y. Ryu, H. Lee, Y. Hong, H. Bandal, M. Goh, H. Kim and J. Lee, Vitrification of Liquid Metal-in-Oil Emulsions Using Nano-Mineral Oxides, *Adv. Mater. Interfaces*, 2023, **10**, 2202527.
53 B. Lombos, P. Sauvageau and C. Sandorfy, The Electronic Spectra of Normal Paraffin Hydrocarbons, *Chem. Phys. Lett.*, 1967, **1**, 42–43.
54 H. Yu, Y. Peng, Y. Yang and Z.-Y. Li, Plasmon-Enhanced Light-Matter Interactions and Applications, *npj Comput. Mater.*, 2019, **5**, 45.
55 B. Yang, C. Li, Z. Wang and Q. Dai, Thermoplasmonics in Solar Energy Conversion: Materials, Nanostructured Designs, and Applications, *Adv. Mater.*, 2022, **34**, 2107351.
56 L. Zhou, Y. Tan, D. Ji, B. Zhu, O. Zhang, J. Xu, Q. Gan, Z. Yu and J. Zhu, Self-Assembly of Highly Efficient, Broadband Plasmonic Absorbers for Solar Steam Generation, *Sci. Adv.*, 2016, **2**, e1501227.

This journal is © The Royal Society of Chemistry 2026